Nanoscale

PAPER

View Article Online
View Journal | View Issue

Enhanced reversible lithium storage in germanium nano-island coated 3D hexagonal bottle-like Si nanorod arrays†

Cite this: *Nanoscale*, 2014, **6**, 1817

Chuang Yue,[a] Yingjian Yu,[a] ZhenGuo Wu,[bc] Xu He,[a] JianYuan Wang,[a] JunTao Li,[c] Cheng Li,[a] Suntao Wu,[a] Jing Li*[a] and Junyong Kang[a]

The rapid development of numerous microscale electronic devices, such as smart dust, micro or nano bio-sensors, medical implants and so on, has induced an urgent demand for integratable micro or nano battery supplies with high energy and power densities. In this work, 3D hexagonal bottle-like Si/Ge composite nanorod (NR) array electrodes with good uniformity and mechanical stability potentially used in micro or nano rechargeable Li-ion batteries (LIBs) were fabricated on Si substrates by a cost-effective, wafer scale and Si-compatible process. The optimized Ge nano-islands coated Si NR composite arrays as anode materials exhibit superior areal capacities and cycling performances by virtue of their favourable structural and improved conductivity features. The unique Si-based composite electrode in nanostructures can be technically and fundamentally employed to configurate all-solid-state Li-ion micro-batteries as on-chip power systems integrated into micro-electronic devices such as M/NEMS devices or autonomous wireless microsystems.

Received 28th September 2013
Accepted 12th November 2013

DOI: 10.1039/c3nr05181a

www.rsc.org/nanoscale

Introduction

In recent years, more and more autonomous electronics are fabricated or commercialized with the rapid development of the integrated circuit (IC) and Micro/Nano-Electronic Mechanical System (M/NEMS) technologies.[1–3] A major characteristic of small microscale components, so called microelectronics or biomedical devices, is that they have to operate independently, implying that a corresponding on-board power system is essential. However, the lagged pace of battery miniaturization hinders the further scaling down or long lasting life of those devices. Traditional 2D planar thin film Li-ion micro-batteries are rapidly emerging but with several potential drawbacks, such as the relatively low energy and power densities and the use of highly reactive lithium metals.[4–7] Therefore, 3D rechargeable LIBs with better electrochemical properties in a small footprint area have been configurated based on 3D current collectors,[8,9] electrodes,[10–12] or electrolytes.[13] Recently, Notten group fabricated a novel 3D-Integrated all-solid-state Li-ion micro-battery using TiN as the Li-ion barrier layer directly coating on high aspect ratio 3D Si trenches or pores, although the performances still need to be improved.[14,15]

Silicon, as an abundant material in the natural world, has been widely used in the field of semiconductor IC technologies and thus turns out to be the best structure support for micro-batteries with the aim to integrate completely with the above micro-electronic autonomous devices and further miniaturize the microsystems. Moreover, Si has outstanding electrochemical properties as the anode material in the applications of LIBs, including high theoretical specific capacity of 3579 mA h g^{-1} ($Li_{15}Si_4$) at room temperature and low working potential (less than 0.5 V *vs.* Li/Li^+).[16–18] Most recently, Ge has also attracted much attention due to its favorable electronic conductivity (2.1 S m^{-1}, 3 orders of magnitude higher than that of silicon at 1.6×10^{-3} S m^{-1}),[19] ionic diffusivity (6.25×10^{-12} cm^2 s^{-1}, 2 orders of magnitude larger than 1.9×10^{-14} cm^2 s^{-1} in silicon),[20] and capacity ($Li_{15}Ge_4$, 1384 mA h g^{-1}).[21,22] It is well accepted that both Si and Ge are good candidates to replace the graphite anode of LIBs but undergo large volumetric expansion upon lithiation/delithiation during cycling.[23,24] In this manner, various technologies, such as vapour–liquid–solid (VLS) or vapour–solid (VS) and so on, have been employed to prepare or synthesise Si, Ge or Si/Ge nanostructures as anodes for LIBs to circumvent the volume expansion induced fracture issues and improve Li-ion kinetics during the electrochemical process.[25–30] But, generally metallic substrates or precursors are required in these procedures, which obstructs the integration with Si-based micro/nano devices.

In this work, the nanosphere lithography (NSL), inductive coupled plasma (ICP) dry etching and ultra-high-vacuum

[a]*Department of Physics/Pen-Tung Sah Institute of Micro-Nano Science and Technology, Xiamen University, Xiamen, Fujian, 361005, China. E-mail: lijing@xmu.edu.cn*
[b]*School of Chemical Engineering, Sichuan University, Chengdu 610 065, China*
[c]*School of Energy Research, State Key Lab of Physical Chemistry of Solid Surfaces, College of Chemistry and Chemical Engineering, Xiamen University, Xiamen 361005, China*

† Electronic supplementary information (ESI) available. See DOI: 10.1039/c3nr05181a

chemical vapor deposition (UHVCVD) techniques were employed to fabricate the 3D hexagonal bottle-like Si NR arrays coated with Ge nano-islands as anodes in LIBs. High discharge capacity and superior rate performance were achieved on this Si/Ge composite electrode, given the optimized 3D NR array structures anchored firmly and orderly on Si substrates and additional single crystalline Ge nano-islands embedded in Si NRs which are beneficial for accommodating the large volume expansion and improving the Li-ion kinetics during Li-ion insertion/extraction processes. The successful fabrication of this unique wafer scale 3D Si-based composite electrode by the cost effective, simple and Si-compatible processes are promising for practical applications in micro/nano-LIBs to power the IC systems, M/NEMS or other electronic devices.

Experimental section

Fabrication of 3D hexagonal Si/Ge NR arrays

Scheme 1 schematically illustrates the fabrication processes of Si/Ge NR arrays. Self-assembled PS nanospheres with the diameter of 360 nm were spin-coated on a silicon substrate in monolayer dispersion and manipulated in size and separation by reactive ion etching (RIE) for 60 s as referred to in our previous procedures.[31] This PS monolayer was then used as the template to produce Si NRs in a commercial ICP (Alcatel-AMS 200) system. During the ICP etching, the alternate gases of SF_6/C_4F_8 (7 s/5 s) were applied for fabricating the hexagonal bottle-like 3D Si NR structures. These chemical species were generated using an RF power of 1000 W at a pressure of 6 mTorr and the duration of the whole process was 8 minutes. The detailed process of the PS nanosphere templates removal can be referred to in our previous work.[31] The Ge nano-islands were then grown on each Si NR's surface in an UHVCVD system at a base pressure of 5×10^{-8} Pa with pure GeH_4 as the precursor at a flow rate of 6 sccm. Before loading into the growth chamber, the wafer patterned with Si NR arrays was cleaned by standard cleaning process and then dried in N_2 ambient. During the growth process, the wafer was heated at 990 °C for 30 min to be de-oxidized followed by Ge nano-islands growth at 400 °C with the chamber pressure of 0.9×10^{-5} Pa and the whole growth time lasting for 30 min.

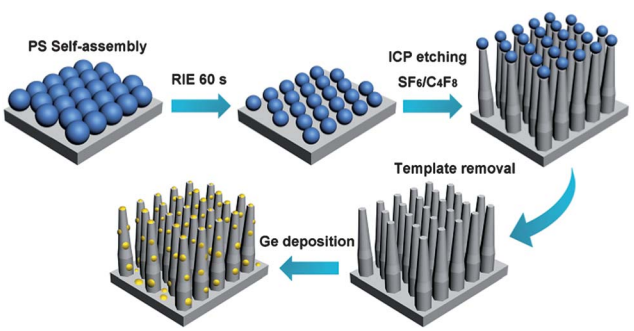

Scheme 1 Illustration of the fabrication processes of Si/Ge NR arrays.

Material characterizations

A Hitachi S-4800 field-emission scanning electron microscope (SEM) with an energy-dispersive X-ray spectrometer (EDX) and JEM-2100 high resolution transmission electron microscope (HRTEM) were employed to observe the morphologies and structures of the Si/Ge NR array samples. The crystal structures of the fabricated samples were characterized by X-ray diffraction (XRD) (Panalytical X'pert PRO) in a 2θ range of 15–55° using Cu-Kα radiation ($\lambda = 1.5406$ Å). The Raman spectra were collected by a Renishaw inVia Raman microscope equipped with a 532 nm laser excitation source.

Electrochemical measurements

The electrochemical performances of these composite NR array electrodes were measured in coin cells (CR 2025), which were assembled in an Ar-filled glove box with the oxygen and water level less than 1 ppm. The current collectors of 20/200 nm Cr/Au were consecutively sputtered on the back sides of the fabricated Si/Ge NR arrays. Then the whole Si/Ge active materials were used as the working electrodes and lithium metal foils as the counter and reference electrodes without using binders and conducting carbon black. A polypropylene (PP) micro-porous film (Cellgard 2400) was chosen as the separator and the electrolyte solution contains 1 M $LiPF_6$ in EC/DEC (1 : 1 in volume) and 2% vinylene carbonate (VC). After the cells were aged for 12 h, CV measurements were recorded on a CHI660D electrochemical workstation (Chenhua, Shanghai) within the voltage window of 0.01–2.0 V *vs.* Li/Li^+ at the scan rate of 0.5 mV s^{-1}. The galvanostatic charge/discharge tests were performed on a LANHE battery program-control test system within the voltage window of 0.13 V to 2.0 V *vs.* Li/Li^+. All the measurements were done at room temperature. The post-testing morphologies of the anode materials were then investigated by SEM from the disassembled coin cells washed by dimethylcarbonate (DMC) in an Ar-filled glove box.

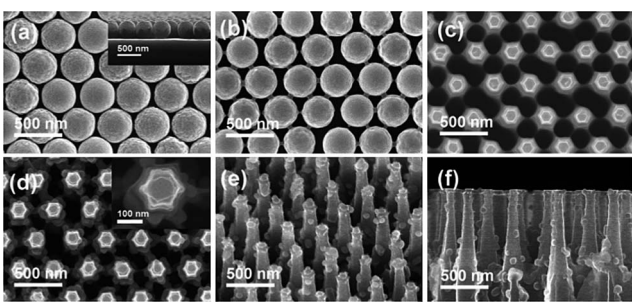

Fig. 1 SEM images of as-fabricated monolayer PS nanosphere templates (a) coating on the Si substrate and (b) then adjusted by O_2 plasma etching for 60 s; (c) planar view of the Si NR arrays produced by the ICP etching process using the corresponding PS nanosphere templates of (b); (d) top, (e) tilt and (f) section views of the Si/Ge NR arrays grown in the UHVCVD system.

Results and discussions

Morphologies and structures

As seen in Fig. 1(a) the two-dimensional PS nanosphere templates with a diameter about 360 nm are hexagonally arranged in monolayer dispersion on the silicon substrate. After the RIE etching for 60 s, the diameter is reduced to about 300 nm as shown in Fig. 1(b) and the corresponding RIE etching rate is about 1 nm s^{-1}. Obviously, the morphology and arrangement of the template remain unchanged while the space between the PS nanospheres is enlarged under the O_2 plasma bombardment. The bridges between the nanospheres in different directions were produced by the plasma etching on the interface of the hexagonally close packed PS nanospheres. As displayed in Fig. 1(c), Si NR arrays with the hexagonal topography were obtained by ICP etching on the Si substrate coated with the PS nanosphere template as in Fig. 1(b). The subsequent Ge growth on the Si NR array patterned substrate was performed by using an UHVCVD technique, which produces Ge nano-islands standing on each individual Si NR with the size ranging from 20 nm to 100 nm as shown in Fig. 1(d–f). The support structure of Si NRs is also revealed in the bottle-like shape with the size of about 200 nm at the bottom and 130 nm at the top. The presence of Ge contents in the EDS characterization evidences the successful deposition of Ge nano-islands in a large area as illustrated in Fig. 2(a and b). It also can be found in the EDS pattern that the Si/Ge NR composite sample contains little O content, which might be due to the surface oxidization in air. The crystal structures of the as-prepared Si/Ge NR composites were examined by XRD as displayed in Fig. 2(c) and the resolved diffraction peaks at 25.4°, 30.3°, 36.2°, 41.7° and 51.4° can be indexed to the Ge (111), (102), (211), (103) and (222) planes (JCPDS card no. 18-0549), respectively. So, the Ge nano-islands with a crystalline property were successfully deposited on these 3D hexagonal bottle-like Si NR arrays. The Raman spectrum of the Si/Ge NR composite was measured at normal incidence with comparison to that of pure Si NR arrays as displayed in Fig. 2(d). The peak located at 520 cm^{-1} for both samples is attributed to the pure Si and a distinguishable peak at about 300 cm^{-1} in Si/Ge NR composite can be assigned to the pure Ge material,[32] which further confirms the Ge composition.

TEM images and the corresponding selective area electron diffraction (SAED) patterns as shown in Fig. 3 were employed to further verify the morphologies and crystal structures of Si/Ge NR composites. Fig. 3(a) shows the part of an individual Si/Ge composite NR, which exhibits a good verticality along the whole length and is decorated with multi Ge nano-islands, while each single island has good contact with the Si NR surface as seen in the high magnification Fig. 3(b). The ordered atom-by-atom alignment in the high resolution TEM image of Fig. 3(c) indicates the high crystal quality of the Ge nano-islands with the interplanar lattice spacing of around 0.36 nm, which corresponds to the (111) plane of Ge. An amorphous-like shell layer can also be visualized on the surface of the Ge nano-island with a thickness of less than 2 nm, which is believed to be due to the surface oxidization in the air indicating a good agreement with the previous EDS result. The SAED pattern in Fig. 3(d) investigated from the marked area of Fig. 3(c) further evidences the single crystallinity of the Ge nano-island. Another TEM image of the Si/Ge NR composite and the corresponding EDS patterns from different areas on the NR surface are displayed in Fig. S1 (ESI†). Besides the nano-islands coated on NRs' surface containing higher Ge content, the exposed surface area also shows Ge composition although the content is low. So, the whole Si NR arrays were epitaxially covered by Ge, which should be beneficial for improving its electrochemical performances due to the

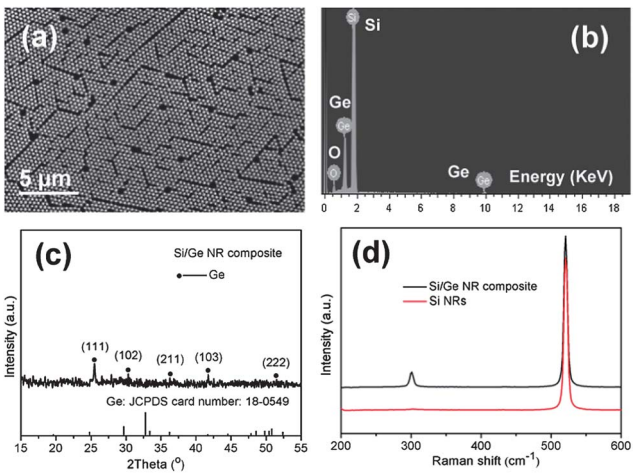

Fig. 2 (a) Top view SEM image of Si/Ge NR arrays in a large area and the corresponding (b) EDS pattern, (c) XRD pattern and (d) Raman spectra, respectively.

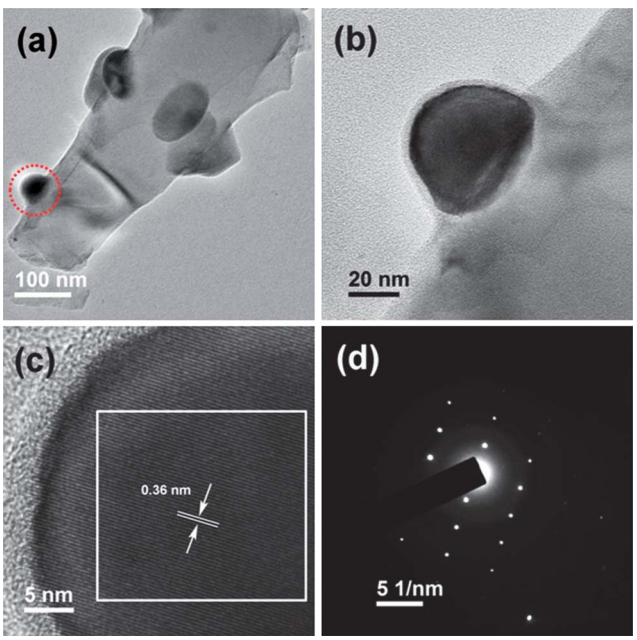

Fig. 3 (a) TEM image of a single Si/Ge composite NR; (b–d) TEM image, HRTEM image and SAED pattern of an individual Ge nano grain taken from the marked area in (a).

intrinsically enhanced surface electrical conductivity and Li ion diffusivity by Ge growth.

Electrochemical properties

The electrochemical properties of the Ge nano-islands deposited Si NR arrays were measured by a half-cell configuration compared with those in the Si NRs sample, as shown in Fig. 4 and S2 (ESI†). The areal capacity (mA h cm^{-2}) is introduced to evaluate the ability of Li-ions inserting/de-inserting in each sample in our manuscript, which is denoted as the total charge/discharge capacity (mA h) divided by the projected surface area (10 mm × 10 mm = 1 cm^2) of the Si/Ge composite electrode. Fig. 4(a) shows the voltage profiles of the Si/Ge NR composite electrode for the first two cycles under the current density of 20 μA cm^{-2}, in which the voltage plateaus during the charge/discharge process are consistent with anodic/catholic current peaks of CV measurements as seen in Fig. S3 (ESI†). The Coulombic efficiency (CE, denoted by the ratio of charge capacity to discharge capacity) for the first two cycles are about 72.7% and 92.8%, respectively. The capacity loss during the first cycle is reasonably proposed to be due to the irreversible Li reaction or the formation of solid state electrolyte interface (SEI) layer, while the ceasing or slowing down of the side reactions are suggested to be responsible for the improved CE afterwards.

The charge/discharge cycling properties with increasing rates up to 200 μA cm^{-2} are shown in Fig. 4(b). The capacity of the Si/Ge NR array anode experiences an obvious drop in the first cycle and then increases in the following several cycles, which is believed to be due to the improved Li-ion diffusion kinetics by an activation and stabilization process.[33–36] At a lower current density of 20 μA cm^{-2} for the first 40 cycles the areal capacity gradually increases and then stabilizes at about 0.6 mA h cm^{-2}, which is much better than 0.3 mA h cm^{-2} of the 3D Si/SnO_2 NR arrays anode in our precious work.[31] This can be ascribed to the fact that the conductive Ge nano-islands play a positive role to improve the electrochemical properties of Si/Ge nanocomposite electrodes by endowing the 3D electronic path, enhancing Li-ion diffusion for fast and stable charge transfer, and lowering the internal electrode resistance during the Li insertion/extraction process. But the slightly smaller CE at about 90% between the 20th and 40th cycles is characterized,

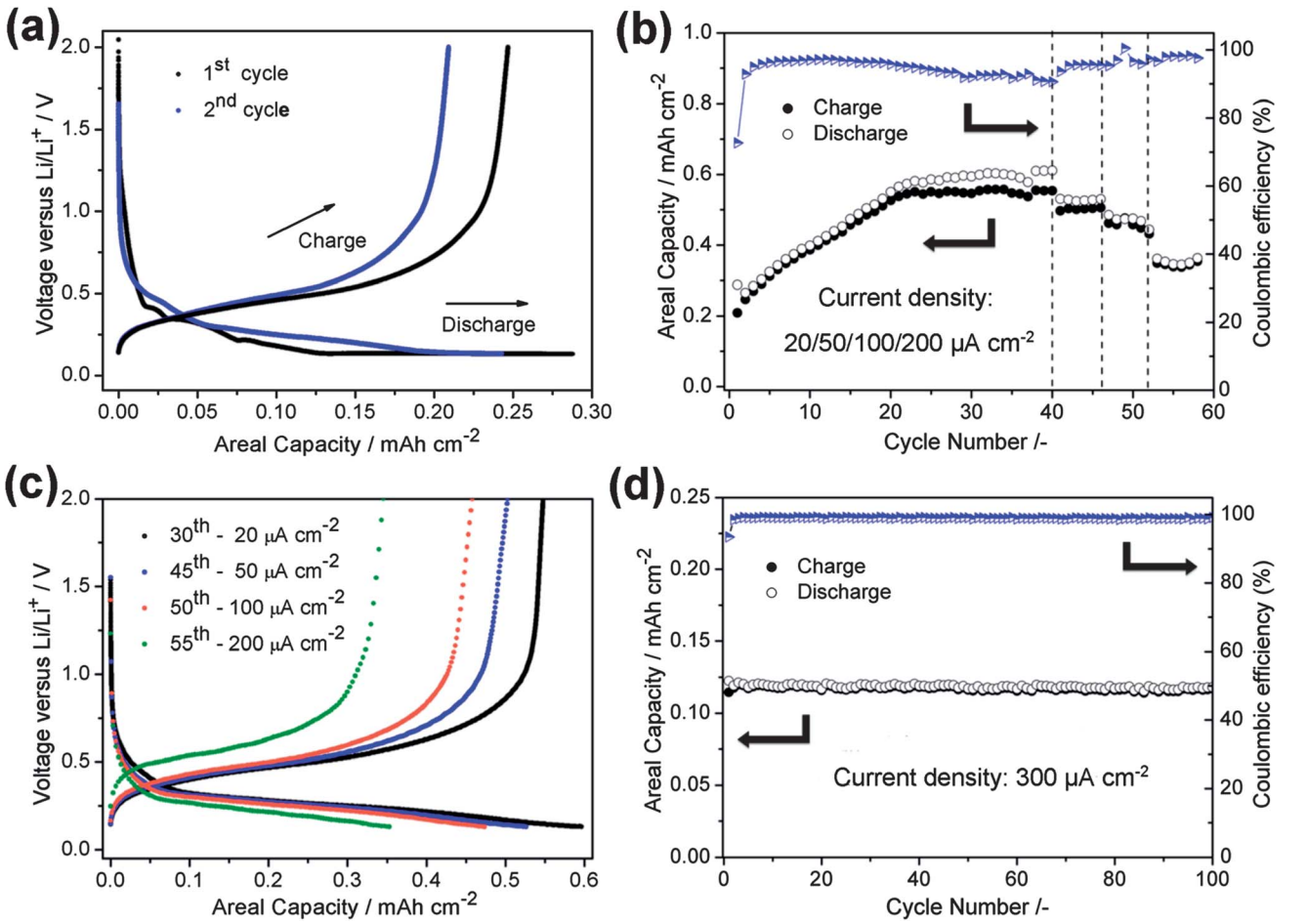

Fig. 4 (a) Voltage profiles for Si/Ge NR composite electrodes during the 1st and the 2nd cycles under a current density of 20 μA cm^{-2} within the voltage window from 0.13 to 2.0 V *vs.* Li/Li^+; (b) the rate capability of Si/Ge NR composite electrodes under different current densities of 20, 50, 100, 200 μA cm^{-2} within the voltage window from 0.13 to 2.0 V *vs.* Li/Li^+ and (c) the corresponding differential capacity *versus* voltage plots; (d) cycling performances of the Si/Ge NR composite electrodes at a current density of 300 μA cm^{-2} within the voltage window between 0.085 and 2.0 V *vs.* Li/Li^+ after the CV measurement for ten cycles.

which can be attributed to the amorphization effects during repeated cycles. And then due to the saturation achievement the CE is improved again during the remaining cycles. On the other hand, when the current density gradually increased to 50, 100 and 200 μA cm^{-2} for each following six cycles, the corresponding areal capacity retention remains at about 90% (0.53 *vs.* 0.6 mA h cm^{-2}), 80% (0.48 *vs.* 0.6 mA h cm^{-2}) and 60% (0.35 *vs.* 0.6 mA h cm^{-2}) respectively, which are competitive by comparing with recent works and meaningful for practical applications.[32,37] The voltage profiles of the Si/Ge NR composite electrodes at different current densities are shown in Fig. 4(c). All the charge/discharge curves exhibit a good flat plateau and high CE characteristics even at the higher current density of 200 μA cm^{-2} (CE: 98%), which is believed to be benefited from the unique 3D bottle-like NR structure and the presence of a single crystalline Ge nanocoating.

Another charge/discharge test at a higher current density of 300 μA cm^{-2} was also conducted on a pre-activated Si/Ge NR composite electrode by a CV measurement process as shown in Fig. 4(d), in which good capacity retention with the areal capacity of about 0.1 mA h cm^{-2} up to 100 cycles can be achieved. There is an understandable capacity drop compared to the sample in Fig. 4(b) due to the damage in the active materials including both the Ge and Si, which is reasonably caused by the higher current density up to 1.0 mA cm^{-2} imposed in the CV measurement (Fig. S3 (ESI†)) and the afterwards cycling at higher current density. The post-testing morphologies of this Si/Ge NR composite anode after 100 cycles were characterized by SEM as seen in Fig. S4 (ESI†). Some volume expansion especially in the lateral direction can be visualized in the cycled Si/Ge NR arrays but the original array layout is still maintained without collapses, which is beneficial for applications of the 3D hexagonal bottle-like Si/Ge NR composite anodes in practical micro power systems. As a result, the reasons for improved electrochemical properties of the Si/Ge NR composites can be summarized as the following: (i) the 3D bottle-like NR arrays, which are generally more mechanically stable than vertical NR arrays on Si substrates, can enlarge the surface area and lower the polarization effects when used as anodes; (ii) the optimized space between the 3D Si/Ge NRs can release the volume expansion during the repeated Li-ion insertion/extraction processes; (iii) single crystal Ge nano-islands coating on the 3D Si NRs can fundamentally improve the surface conductivity and Li ion diffusion, and thus enhance the cycle performance. Therefore, the combination of this unique 3D Si NR structure and the shell layer of Ge nano-islands can effectively improve the active material's electrochemical properties by mutual promotion effects.

Conclusion

In summary, 3D hexagonal bottle-like Si NR arrays decorated by single-crystalline Ge nano-islands were successfully fabricated as anode materials for applications in lab on-chip micro/nano LIBs. The enhanced Li ion diffusivity and good electronic conductivity induced by the growth of Ge nano-islands in this 3D composite structure are responsible for the improved electrochemical properties. This low cost and Si-compatible process of NSL-ICP dry etching technique combined with UHVCVD technique are promising to build wafer scale integrated all-solid-state Li-ion microbattery systems and find potential applications in autonomously powered micro/nano electronics, such as M/NEMS devices, smart dusts, and biomedical devices, and so on.

Acknowledgements

This work is financially supported by the MOST of China under the 973 programs (2009CB930704), National Natural Science Foundation of China (61106118), Science and Technology Project of Fujian Province of China (2013H0046), Natural Science Foundation of Fujian Province of China (2011J01362), and Fundamental Research Funds for the Central Universities (2011121026).

Notes and references

1 J. W. Long, B. Dunn, D. R. Rolison and H. S. White, *Chem. Rev.*, 2004, **104**, 4463–4492.
2 T. S. Arthur, D. J. Bates, N. Cirigliano, D. C. Johnson, P. Malati, J. M. Mosby, E. Perre, M. T. Rawls, A. L. Prieto and B. Dunn, *MRS Bull.*, 2011, **36**, 523–531.
3 K. Palem and A. Lingamneni, *IEEE DAC.*, 2012, 924–929.
4 J. B. Bates, N. J. Dudney, B. Neudecker, A. Ueda and C. D. Evans, *Solid State Ionics*, 2000, **135**, 33–45.
5 N. J. Dudney, *Mater. Sci. Eng., B*, 2005, **116**, 245–249.
6 B. Dunn, J. W. Long and D. R. Rolison, *Electrochem. Soc. Interface*, 2008, **17**, 49–53.
7 J. F. M. Oudenhoven, R. J. M. Vullers and R. van Schaijk, *Int. J. Energy Res.*, 2012, **36**, 1139–1150.
8 S. K. Cheah, E. Perre, M. Rooth, M. Fondell, A. Hårsta, L. Nyholm, M. Boman, T. Gustafsson, J. Lu, P. Simon and K. Edstrom, *Nano Lett.*, 2009, **9**, 3230–3233.
9 S. R. Gowda, A. L. Mohana Reddy, X. Zhan, H. R. Jafry and P. M. Ajayan, *Nano Lett.*, 2012, **12**, 1198–1202.
10 C. Wang, L. Taherabadi, G. Jia, M. Madou, Y. Yeh and B. Dunn, *Electrochem. Solid-State Lett.*, 2004, **7**, 435–438.
11 S. R. Gowda, A. L. Mohana Reddy, M. M. Shaijumon, X. Zhan, L. Ci and P. M. Ajayan, *Nano Lett.*, 2011, **11**, 101–106.
12 T. Djenizian, I. Hanzu and P. Knauth, *J. Mater. Chem.*, 2011, **21**, 9925–9937.
13 M. Kotobuki, Y. Suzuki, H. Munakata, K. Kanamura, Y. Sato, K. Yamamoto and T. Yoshida, *J. Electrochem. Soc.*, 2010, **157**, 493–498.
14 J. F. M. Oudenhoven, L. Baggetto and P. H. L. Notten, *Adv. Energy Mater.*, 2011, **1**, 10–33.
15 L. Baggetto, H. C. M. Knoops, R. A. H. Niessen, W. M. M. Kessels and P. H. L. Notten, *J. Mater. Chem.*, 2010, **20**, 3703–3708.
16 R. A. Sharma and R. N. Seefurth, *J. Electrochem. Soc.*, 1976, **123**, 1763–1768.
17 M. N. Obrovac and L. Christensen, *Electrochem. Solid-State Lett.*, 2004, **7**, 93–96.

18 T. D. Hatchard and J. R. Dahn, *J. Electrochem. Soc.*, 2004, **151**, 838–842.
19 E. M. Conwell, *Proc. Inst. Radio Eng.*, 1952, **40**, 1327–1337.
20 C. S. Fuller and J. C. Severiens, *Phys. Rev.*, 1954, **96**, 21–24.
21 L. Baggetto and P. H. L. Notten, *J. Electrochem. Soc.*, 2009, **156**, 169–175.
22 A. Jain, E. Kawasako, H. Miyaoka, T. Ma, S. Isobe, T. Ichikawa and Y. Kojima, *J. Phys. Chem. C*, 2013, **117**, 5650–5657.
23 X. H. Liu, L. Zhong, S. Huang, S. X. Mao, T. Zhu and J. Y. Huang, *ACS Nano*, 2012, **6**, 1522–1531.
24 X. Hua Liu, S. Huang, S. Tom Picraux, J. Li, T. Zhu and J. Yu Huang, *Nano Lett.*, 2011, **11**, 3991–3997.
25 C. K. Chan, H. Peng, G. Liu, K. McIlwrath, X. F. Zhang, R. A. Huggins and Y. Cui, *Nat. Nanotechnol.*, 2008, **3**, 31–35.
26 Li-F. Cui, R. Ruffo, C. K. Chan, H. Peng and Y. Cui, *Nano Lett.*, 2009, **9**, 491–495.
27 J. Wang, N. Du, H. Zhang, J. Yu and D. Yang, *J. Mater. Chem.*, 2012, **22**, 1511–1515.
28 M.-H. Seo, M. Park, K. Tae Lee, K. Kim, J. Kim and J. Cho, *Energy Environ. Sci.*, 2011, **4**, 425–428.
29 X. Li, X. Meng, J. Liu, D. Geng, Y. Zhang, M. N. Banis, Y. Li, J. Yang, R. Li, X. Sun, M. Cai and M. W. Verbrugge, *Adv. Funct. Mater.*, 2012, **22**, 1647–1654.
30 X. Li, Y. Zhong, M. Cai, M. P. Balogh, D. Wang, Y. Zhang, R. Li and X. Sun, *Electrochim. Acta*, 2013, **89**, 387–393.
31 C. Yue, Y. Yu, J. Yin, T. Wong, Y. Zang, J. Li and J. Kang, *J. Mater. Chem. A*, 2013, **1**, 7896–7904.
32 P. R. Abel, A. M. Chockla, Y.-M. Lin, V. C. Holmberg, J. T. Harris, B. A. Korgel, A. Heller and C. B. Mullins, *ACS Nano*, 2013, **7**, 2249–2257.
33 Z. Hong and M. Wei, *J. Mater. Chem. A*, 2013, **1**, 4403–4414.
34 L. Zeng, C. Zheng, L. Xia, Y. Wang and M. Wei, *J. Mater. Chem. A*, 2013, **1**, 4293–4299.
35 X. Li, A. Dhanabalan, L. Gu and C. Wang, *Adv. Energy Mater.*, 2012, **2**, 238–244.
36 X. Li and C. Wang, *J. Mater. Chem. A*, 2013, **1**, 165–182.
37 T. Song, H. Cheng, H. Choi, J.-H. Lee, H. Han, D. H. Lee, D. S. Yoo, M.-S. Kwon, J.-M. Choi, S. G. Doo, H. Chang, J. Xiao, Y. Huang, W. I. Park, Y.-C. Chung, H. Kim, J. A. Rogers and U. Paik, *ACS Nano*, 2012, **6**, 303–309.